Saturated absorption spectroscopy of $M1$ transitions of O_2 near 764 nm

Y.-R. Xu,[1] A.-W. Liu,[1,2,3,*] Y. Tan,[4] C.-L. Hu,[4] and S.-M. Hu[1,2,3]

[1]*Department of Chemical Physics, University of Science and Technology of China, Hefei 230026, China*
[2]*Hefei National Laboratory, University of Science and Technology of China, Hefei 230088, China*
[3]*State Key Laboratory of Molecular Reaction Dynamics, University of Science and Technology of China, Hefei 230026, China*
[4]*Hefei National Research Center for Physical Sciences at Microscale, University of Science and Technology of China, Hefei 230026, China*

(Received 25 July 2023; revised 18 March 2024; accepted 20 March 2024; published 8 April 2024)

Magnetic dipole transitions of oxygen molecules, which span the microwave-to-infrared region, play a crucial role in remote sensing applications. However, accurately determining the parameters of these weak transitions has long been a challenge. In this work, we present a saturated absorption spectroscopy measurement of magnetic dipole transitions of $^{16}O_2$ near 764 nm using a comb-locked cavity ring-down spectrometer. The Line positions of eight transitions in the P branch of the $b\,^1\Sigma_g^+ \leftarrow X\,^3\Sigma_g^-(0,0)$ band were determined with an accuracy of better than 3.5 kHz under zero magnetic field, an improvement of two orders of magnitude over previous studies. Zeeman splittings induced by the Earth's geomagnetic field were partially resolved, and their influence on the spectral line profile was meticulously analyzed using the Stokes matrix formalism. The results of this study also indicate the potential for the experimental determination of the Landé g factors of the energies of O_2 with better accuracy.

DOI: 10.1103/PhysRevA.109.042809

I. INTRODUCTION

As an essential component of the Earth's atmosphere, the role of molecular oxygen in geochemical and biological processes [1–3] motivates long-term observations in a wide variety of scientific and environmental research [4,5]. Techniques based on absorption spectroscopy provide direct and noninvasive measurements. However, only weak magnetic dipole and electric quadrupole transitions are allowed from the ground state ($X\,^3\Sigma_g^-$) of oxygen in the microwave region to the infrared region. Various highly sensitive spectroscopic techniques [6–10] have been developed for the trace detection of O_2. Meanwhile, due to its wide dynamic range and regular spectral line distribution, atmospheric oxygen absorption has been extensively included in various remote sensing missions, such as GOME [11], OCO-2/3 [12], GOSAT [13], TANSAT [14], and TCCON [15]. The oxygen spectra are used to extract a variety of atmospheric data, such as the cloud top height, cloud optical depth, surface pressure, atmospheric pressure profile, upper atmospheric temperature profile, aerosol profile, and surface albedo. Microwave radiometers [16] and Limb sounders (EOS aura/mls) [17] can also remotely measure the distribution of the geomagnetic field using the oxygen Zeeman effect, which was discovered as a critical factor in the radiative transfer model [18–21] to extend the atmospheric temperature measurements to altitudes up to 55 km [22–25]. Applications of oxygen remote sensing in atmospheric science, in turn, encourage more high-precision spectroscopic studies of O_2.

Decades after Babcock and Herzberg's first observation of oxygen absorption spectroscopy in 1948 [26], O'Keefe and Deacon measured the Doppler-limited absorption spectroscopy of the A band of oxygen using cavity ring-down spectroscopy (CRDS) [27]. It was also the first demonstration of the CRDS technique that is extensively applied in many fields nowadays.

In particular, the development of frequency-stabilized cavity ring-down spectrometers has led to significant improvements in the precision of line profile parameters [28–33]. These include the sub-MHz line positions [28,29], line intensities of transitions with J values up to 51 [30], and line mixing parameters at the A- and B-band heads [32,33]. The Einstein A coefficients of magnetic dipole ($M1$) and electric quadrupole ($E2$) transitions are $10^{-14} \sim 10^{-9}$ of those allowed electric dipole ($E1$) transitions between electronic states [34]. So far, only Doppler-free saturated absorption spectroscopy (SAS) of the H_2 electric quadrupole transition has been reported very recently [35], and no SAS measurements of the magnetic dipole transitions. Extremely high requirements for optical intensity and detection sensitivity prevent the determination of the Landé g factors of the oxygen rotational energy states in the $X\,^3\Sigma_g^-$ state by SAS measured at a magnetic field of several Gauss. These factors greatly influence the accurate evaluation of the unpolarized cross section and brightness temperature from remote sensing observations using oxygen microwave spectroscopy [36]. Meanwhile, the accurate Landé g factors of molecular rovibrational states can also be used as a benchmark to test the spin-spin interaction in the Hamiltonian model, with deviations of up to 15% in the calculated values for different Hamiltonian models [37].

Compared to microwave transitions from $X\,^3\Sigma_g^-$ states, rovibrational transitions from the same low electronic state in the A or B bands of oxygen are better suited for the experimental determination of the Landé g factors because the upper singlet electronic states are immune to the Zeeman effect.

*awliu@ustc.edu.cn

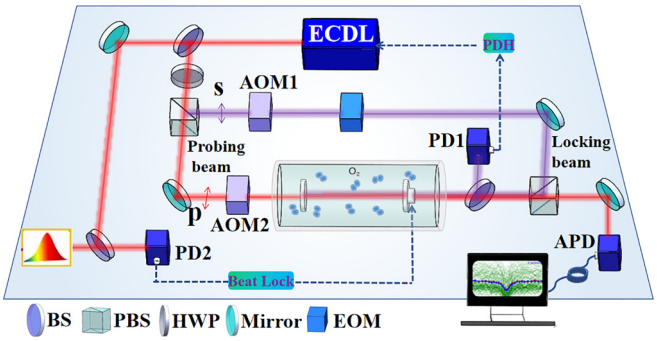

FIG. 1. Configuration of the saturated cavity ring-down spectroscopy apparatus. BS: beam splitter; PBS: polarized beam splitter; HWP: half-wave plate; AOM: acoustic-optic modulator; EOM: electro-optic modulator; PZT: piezoelectric ceramic actuator; PD: photodiode; APD: Avalanche photodiode.

A comb-locked cavity ring-down spectrometer centered at 780 nm has recently been developed in our laboratory, which combines a sensitivity (the minimum detectable absorption coefficient) on the order of 10^{-11} cm^{-1}, a frequency resolution of a few kHz and an intracavity intensity of several kW/cm^2 as other similar setups in the near-infrared region [38,39]. With this spectrometer, we are able to observe the SAS of oxygen magnetic dipole transitions with saturation intensities above 30 kW/cm^2. Line positions were determined with an accuracy of 3.5 kHz for eight transitions in the range 763.7–765.2 nm under geomagnetic field shielding. Discrepancies between the SAS values and those obtained from Doppler-limited measurements are discussed, as well as microwave frequency comparisons between the values calculated in this work and those reported in the literature. We also study the Lamb-dip spectra of these transitions under geomagnetic field, using the Stokes matrix formalism to analyze the influence of the Zeeman effect on the spectral profile.

II. EXPERIMENTS

The comb-locked cavity ring-down spectrometer is schematically shown in Fig. 1. The optical layout is similar to those used in our previous work [38,40]. A high-finesse optical resonant cavity is used to increase both the effective absorption path length and the intracavity laser power by a factor of over 10^3. The laser source is an external cavity diode laser (ECDL, Toptica DL Pro100) tunable in the range of 763 to 805 nm. One beam from the laser, noted as the "locking beam," is first shifted by an acoustic-optic modulator AOM1 in Fig. 1, then phase-modulated by an electrooptical modulator (EOM), and used to lock to a high-finesse cavity with the Pound-Drever-Hall (PDH) method. The optical cavity is composed of two mirrors with a reflectivity of $R = 99.995\%$ at 760 to 810 nm (Layertec GmbH Inc.). The distance between the two mirrors is 70.3 cm, corresponding to a free spectral range (FSR) of 213.1 MHz. The cavity is installed in a stainless-steel chamber pumped by a turbo pump, and the leaking rate of the chamber is below 0.2 Pa/day. Another beam from the laser, denoted as the "probing beam," is frequency shifted by another acoustooptic modulator (AOM2 in Fig. 1), and then coupled into the cavity for CRDS measurements. Its frequency is shifted by one FSR of the cavity from the "locking" beam. Consequently, the probing beam will pass through the cavity when the locking servo loop is closed. The polarization of the probing beam is set perpendicular to the locking beam to avoid crosstalk between the two beams.

The beat frequency between the locking beam and an optical frequency comb (OFC) is recorded to calibrate the laser frequency. One of the cavity mirrors is attached to a piezoelectric ceramic actuator (PZT), and a locking loop is used to stabilize the cavity length according to the beat frequency. The optical comb is the second harmonic generation of a 1520-nm Yb-dopped comb with a repetition frequency f_r of 205 MHz and a carrier frequency f_0 of 250 MHz referenced to a local active hydrogen maser (VCH-1003M). The drift of the maser has been measured to be below 2×10^{-13} s^{-1}. The overall uncertainty of the comb teeth frequency has been determined to be less than 0.3 kHz. The absolute frequency of our probe light can be expressed as

$$\nu = 2f_0 + nf_r + f_A + f_B, \tag{1}$$

where f_A is the frequency shift of AOM2, f_B is the beat frequency between the optical comb and the laser, and the integer n represents the comb tooth index. Laser scanning is implemented by changing the frequency f_B.

The beam waist radius is about 0.5 mm. About 3-mW incident laser power was used for the measurements of the Lamb dips. The unidirectional laser power inside the vacuum cavity was estimated to be about 9 W according to the transmittance of the cavity [41]. Ring-down events were generated by periodically chopping the "probe" beam with AOM2. The ring-down curve recorded by an acquisition card was fit by a single exponential decay function to derive the ring-down time τ. The absorption coefficient of the sample gas was obtained as $\alpha = \frac{1}{c\tau} - \frac{1}{c\tau_0}$, where τ_0 is the ring-down time without absorption and c is the speed of light.

An oxygen gas sample (purity >99 %) was used in the experiment without further purification. The temperature of the sample cell was stabilized at 298.15 K and the temperature drift was less than 50 mK/day.

III. RESULTS AND DISCUSSION

The studied O_2 lines near 764 nm are magnetic dipole transitions in the P branch of the $b\,^1\Sigma_g^-$ ($v=0$)–$X\,^3\Sigma_g^-$ (v=0) band. Under Hund's case [Fig. 2(b)] coupling scheme, a rovibrational energy level can be denoted by three quantum numbers: S, N, and J, where S is the spin angular momentum, N is the rotational angular momentum, and J is the total angular momentum. Due to the spin-rotation coupling, the energy level with rotational quantum number N in the triplet state $X\,^3\Sigma_g^-$ splits into three sublevels ($J = N - 1, N, N + 1$) for $N > 1$, while the singlet state $b\,^1\Sigma_g^+$ has $J = N$. Therefore, there are four branches, ^PP, ^PQ, ^RQ, and ^RR in the vibrational band. They are illustrated in Fig. 2(a). Transitions studied in this work are also indicated in Fig. 2(b) together with the line intensity given in the HITRAN2020 datatbase [42].

Figure 3 shows the saturated absorption spectra of the $^PQ(10)$ and $^PP(11)$ lines recorded at a sample pressure of

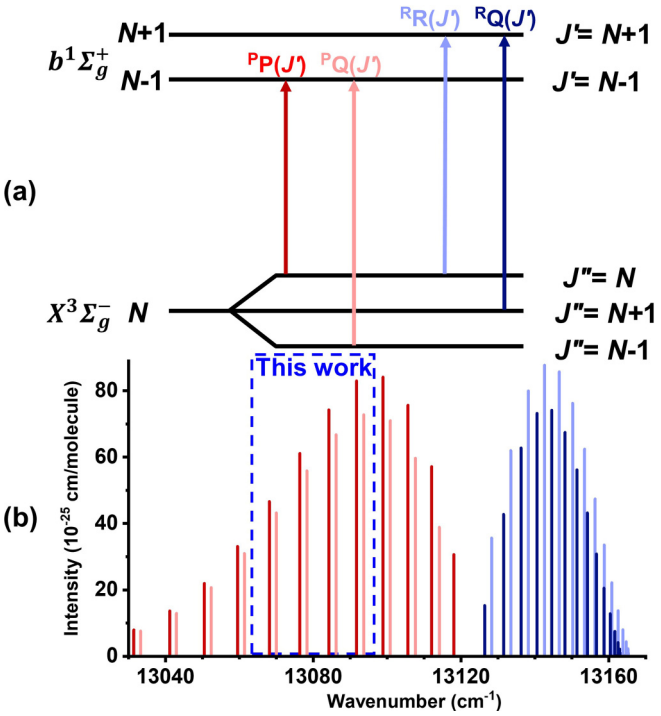

FIG. 2. (a) Energy level diagram of the A band transitions of $^{16}O_2$. (b) Overview of the A band of O_2 near 760 nm. The rectangle indicates eight lines studied in this work.

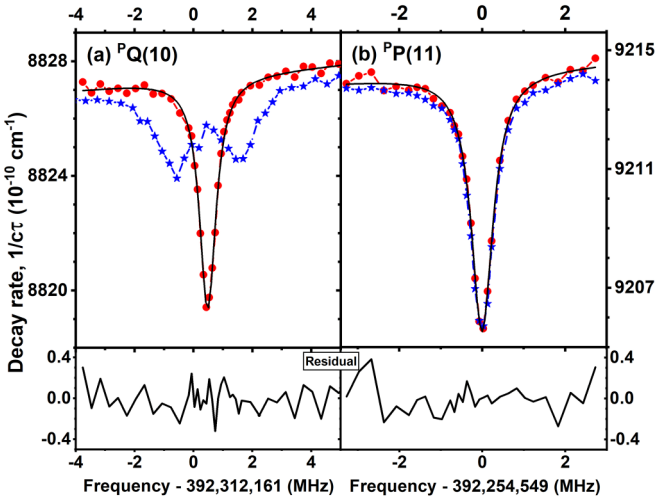

FIG. 3. Saturated absorption spectra of the $^PQ(10)$ and $^PP(11)$ transitions. Red points are experimental data recorded with magnetic shielding, and they were fitted with the following function: $\frac{1}{c\tau} = A + B(\nu - \nu_0) + \frac{2C}{\pi}\frac{w}{4(\nu-\nu_0)^2+w^2}$, where A and B represent the intercept and slope of the baseline, C is the integral of the absorption coefficient, w is the full width at half maximum (FWHM) of the peak, and ν_0 is the central frequency of the line. Solid black lines are simulated spectra and the fitting residuals are shown in the lower panels. Blue points show the experimental data recorded under the geomagnetic field (31°50′34″N, 117°15′12″E) on April 9, 2022, 0.55 Gauss, without using magnetic shielding. Oxygen sample pressure: 2 Pa. Number of scan: 518.

about 2 Pa. Red and blue dots indicate spectra recorded with and without magnetic shielding, respectively. The spectra recorded with magnetic shielding were fitted with Lorentzian functions (solid black lines), and the fit residuals are shown in the lower panels. The signal-to-noise ratio is around 30 : 1 for a spectrum averaged with about 100 scans, with each scan accomplished in about 30 s.

With the magnetic shield applied, a single peak is observed which could be fitted by a Lorentzian function with a linewidth of 0.58 MHz (full width at half maximum). Under the geomagnetic field, the spectrum shows two bumps that could be fitted with Lorentzian peaks with widths of 1.3 MHz and 1.5 MHz, respectively, and the distance between the two bumps is about 2 MHz. Other lines in the ^PQ branch show similar profiles as the $^PQ(10)$ line shown in Fig. 3.

A. Line positions under zero magnetic field

To eliminate the influence of geomagnetic fields on the lineshape of the oxygen $M1$ transition, the chamber was covered with multiple layers of permalloy. The residual magnetic field in the optical cavity was found to be less than 0.05 Gauss. For a ^PQ transition, only one peak was observed under the zero magnetic field, but a broad feature with double peaks was observed when the magnetic shield was removed (discussion in the next subsection), as shown in Fig. 3. It allows us to determine the line position with a statistical uncertainty of less than 3 kHz. In total, we determine the positions of eight lines in four pairs. Each pair shares the same upper level.

Similar to the studies we carried out for some other molecules such as $^{12}C\,^{16}O$ [38], $^{12}C_2\,H_2$ [40], and CO_2 [39], systematic uncertainties were investigated, including those from the frequency comb, the drift of AOM, the frequency shift induced by laser power and sample pressure, the possible asymmetry in the line profile, and the second-order Doppler shift. The frequency drift of AOM2 is about 0.05 kHz. Lamb-dip spectra of $^PP(11)$ were recorded at different sample pressures and different laser powers to determine the power- and pressure-induced shifts. The upper panel of Fig. 4 shows Lamb-dip spectra recorded with various laser powers (a) and at different oxygen pressures (b). The saturation parameter S was estimated as the ratio between the intracavity laser power and the saturation power [43]. As the laser power changes during a ring-down event, we adopted an effective S value according to the averaged amplitude of the RD signal included in the single exponential decay fit. A noticeable augmentation was observed in both the dip depth and linewidth as the laser power and sample pressure increased. The pressure-broadening coefficient of $^PP(11)$ was measured to be 124(11) kHz/Pa, which is approximately seven times greater than the value of 15.1 kHz/Pa given in the HITRAN2020 database [42]. Similar pressure dependence was also found for the other seven lines studied in this work. Note that the pressure-broadening coefficients given in the HITRAN database were determined from Doppler-limited spectroscopy recorded under moderate pressures (typically 10^3–10^5 Pa), they could be significantly less than those obtained from SAS measurement at much lower pressures. This effect has been observed in a number of studies for various molecules [38–40,44,45]. Further quantitative analysis on the pressure-broadening ef-

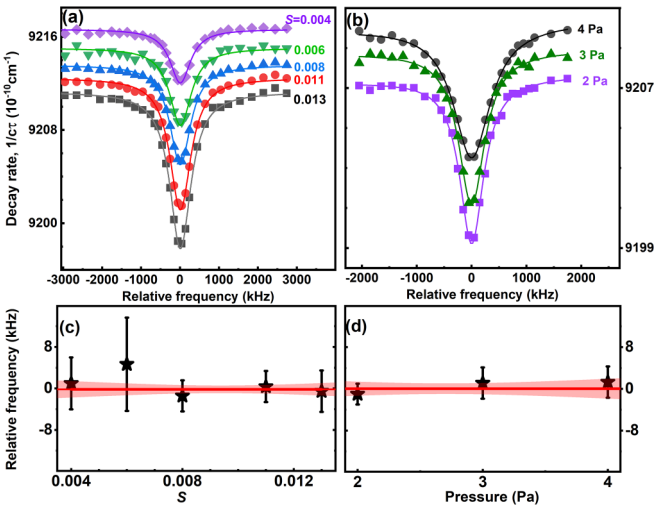

FIG. 4. Upper panels: Cavity ring-down saturation spectra of the $^PP(11)$ line retrieved with (a) various laser powers (Sample pressure: 3.0 Pa) and (b) at different sample pressures. Spectra were vertically shifted for a better illustration. Lower panels: (c) Line centers obtained at different effective saturated coefficients S, (d) line centers obtained at different sample pressures. Red shadows show the 68% confidence intervals of the linear fit. Note that the effective S value was derived using the average laser power of the ring-down curve used in the single-exponential decay fitting, and all frequencies are shifted by 392 254 548 991.1 kHz.

fect requires better control of the incident laser power applied in the measurements.

The lower panel of Fig. 4(c) shows the line centers acquired at different laser powers, and the power shift is determined to be negligible. Spectra obtained at different pressures within the range of 2 to 4 Pa show that the pressure-induced shift is also negligible with in an uncertainty of about 1.2 kHz, as shown in Fig. 4(d). Note that the pressure-induced shifts are about −1.5 kHz/Pa for eight transitions in the Doppler regime [46]. As discussed in our previous studies [38–40], we estimated the uncertainty within the frequency range of 0.1–1.4 kHz to account for potential asymmetry in the line profile model. The second-order Doppler shift, taking the most probable gas velocity of 392 m/s of $^{16}O_2$ at 298 K, is estimated to be −0.32 kHz with an uncertainty below 10 Hz. The recoil-induced doublet of 20 kHz difference [47] results in symmetry spectral broadening, leaving no recoil shift. The overall uncertainties are below 3.5 kHz for eight lines in the oxygen A band near 764 nm. Their frequencies together with the uncertainties are given in the third column of Table I.

For comparison, sub-MHz accurate values obtained from Doppler-limited spectroscopy [28] are also given in the second column. Note that line positions given by Yu *et al.* [48] are calculated from an empirical global fit, identical to that in the HITRAN2020 database [42]. Discrepancies between the literature values and our frequencies are found to be below 0.5 MHz, falling within the range of uncertainties given in Ref. [28]. The average difference between the line positions in the HITRAN2020 database [42] and our values is 0.54 MHz. This deviation exceeds the accuracy range (0.03–0.3 MHz) evaluated by the HITRAN group. As shown in Fig. 2, the ^PP and ^PQ transitions share the same upper levels $J = N - 1$ in the $b^1\Sigma_g^+$ electronic state. Their frequency difference $\delta\nu$ therefore represents the energy difference in the ground state, which can be measured directly by microwave spectroscopy. The energy difference $\delta\nu_{\rm this}$, determined in this work, is presented in the fourth column of Table I, together with a comparison with the values obtained from microwave spectroscopy $\delta\nu_{\rm MW}$ [49]. The discrepancies $\Delta = \delta\nu_{\rm this} - \delta\nu_{\rm MW}$ are all below 4 kHz, in agreement with the combined experimental uncertainty.

B. Zeeman splittings under geomagnetic field

The geomagnetic field removes the Zeeman degeneracy of the ground triplet state $^3\Sigma_g^-$ of O_2, while the $^1\Sigma_g^+$ state remains degenerate. Each Zeeman component in the ground electronic state has a frequency shift in a magnetic field

$$\Delta\nu_Z = -Mg(J)\frac{\mu_B B}{h}. \tag{2}$$

Here B is the magnitude of the magnetic field, μ_B is the Bohr magneton, $M = -J, -J+1, \ldots, J$, is the quantum number of J projected along the direction of the magnetic field, and $g(J)$ is the Landé factor. The magnetic dipole transition se-

TABLE I. Frequency centers (under the zero magnetic field) of the transitions in the A band of $^{16}O_2$, unit in kHz. Numbers in parentheses represent 1σ uncertainties in the last quoted digit.

	Frequency, ν		$\delta\nu$ [a]		
Transition	Doppler [28]	This work	This work	Microwave	Δ[b]
$^PQ(8)$	392 537 926 760(720)	392 537 926 288.4(18)	58 323 877.7(25)	58 323 876.6(17)	1.1(30)
$^PP(9)$	392 479 602 760(690)	392 479 602 410.7(18)			
$^PQ(10)$	392 312 161 930(660)	392 312 161 477.0(21)	57 612 486.1(40)	57 612 483.4(05)	2.7(40)
$^PP(11)$	392 254 549 230(630)	392 254 548 990.9(33)			
$^PQ(12)$	392 075 397 630(600)	392 075 397 631.2(20)	56 968 208.3(37)	56 968 207.7(15)	0.6(40)
$^PP(13)$	392 018 429 960(600)	392 018 429 422.9(31)			
$^PQ(14)$	391 827 599 710(600)	391 827 599 805.7(15)	56 363 394.6(23)	56 363 398.3(16)	−3.7(28)
$^PP(15)$	391 771 236 450(570)	391 771 236 411.2(17)			

[a]Energy difference in the ground state, $\delta\nu = \nu[^PQ(J-1)] - \nu[^PP(J)] = E''(N,J) - E''(N,J-1)$.

[b] Difference between $\delta\nu$ obtained from this work and that from the microwave spectroscopy [49], $\Delta = \delta\nu_{\rm this} - \delta\nu_{\rm MW}$.

lection rule follows $\Delta M = 0, \pm 1$, corresponding to π and $\sigma_\pm$ transitions, respectively.

Taking the Hund's case [Fig. 2(b)] description of the ground state $X^3\Sigma_g^-$, the factor $g(J)$ is roughly equal to $2/[J(J+1)]$ and $-2/J$ for the transitions in the ${}^PP$ and ${}^PQ$ branches, respectively [37]. The distance between nearby Zeeman components for a ${}^PP(J'')$ ($J'' = 9, 11, 13, 15$) transition is expected to be in the range of 5–15 kHz under the geomagnetic field of 0.55 Gauss. It is only 2% of the measured linewidth and is unresolved in our measurements. As shown in the right panel of Fig. 3, the linewidth of the ${}^PP(11)$ line in the local geomagnetic field is only slightly larger than that recorded with magnetic shielding. Analogous behaviors were observed for the three other lines in the ${}^PP$ branch.

The Landé factor $g(J)$ for the ${}^PQ$ branch is approximately ten times larger than that for the ${}^PP$ branch [37]. It leads to a Zeeman splitting up to a few hundred kilohertz and a broad feature with two peaks under the geomagnetic field, as shown in the left panel of Fig. 3. For a transition in the ${}^PQ$ branch, we have $\Delta J = 0$, and the intensity of each M component is given by [50]

$$S_\pi = \frac{3M^2}{J(J+1)(2J+1)},$$
$$S_{\sigma_\pm} = \frac{3(J \mp M)(J+1 \pm M)}{2J(J+1)(2J+1)}. \tag{3}$$

Consequently, the intensities of different Zeeman components are related to the direction of the magnetic field, the propagation, and the polarization of the radiation. Quantitative investigations of Zeeman transitions have been established for cases where the magnetic field is parallel or perpendicular to the light-propagating direction, and the Faraday model and Voigt model are used in these two cases, respectively [22,51,52]. However, when there is an angle between the magnetic field and the direction of light propagation, one cannot simply decompose the magnetic field into two directions and use separate models for quantitative analysis.

The Zeeman effect in the atmospheric radiative transfer has been analytically derived with both coherency [53,54] and Stokes formalisms [55,56]. The latter is widely adopted by the solar physics community to study the magnetic field of stars [57,58]. Atmospheric radiative transfer simulator (ARTS) [59,60] uses the Stokes formalism and has been successfully applied to verify ground-based microwave radiometer measurements [22]. Here we use this formalism to analyze the saturated spectrum of O_2 under the geomagnetic field. According to the results given in the Appendix, the total light intensity [Eq. (A1)] can be expressed as

$$I \propto \tfrac{1}{2}\phi_\pi \sin^2\theta + \tfrac{1}{4}(\phi_{\sigma_+} + \phi_{\sigma_-})(1 + \cos^2\theta) + \tfrac{1}{2}[\phi_\pi - \tfrac{1}{2}(\phi_{\sigma_+} + \phi_{\sigma_-})]\sin^2\theta \cos 2\eta, \tag{4}$$

where $\phi_{\pi,\sigma_\pm}$ represent the absorption for π, σ_+, and σ_- transitions, as defined by Eq. (A4) in the Appendix.

In Eq. (4), θ denotes the angle between the magnetic field vector $\vec{B}$ and the z axis, and η is the angle between the y axis and the projection of $\vec{B}$ in the xy plane, as shown in Fig. 5, where the xz plane is horizontal and the laser propagates along the z axis. The local geomagnetic field

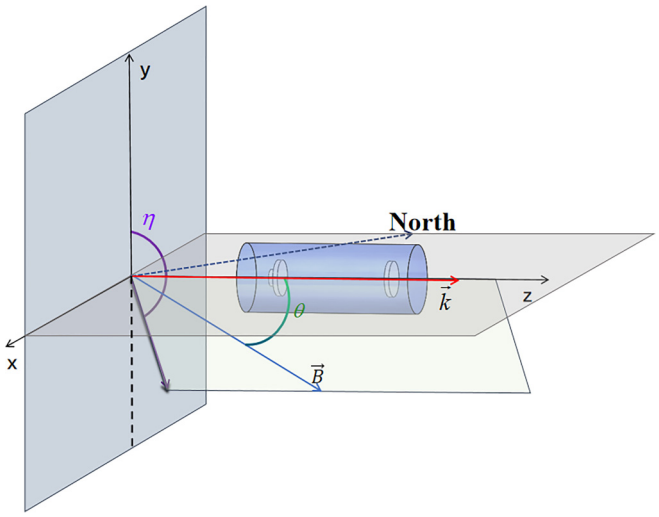

FIG. 5. Definition of the reference frame. The laser propagates along the z axis, which is linearly polarized along the x axis. The local geomagnetic vector $\vec{B}$ is 0.55 Gauss with $\theta = 56^\circ$ and $\eta = 157^\circ$.

was measured by a TESLA meter TM-801EXP. The field has an amplitude of 0.55 Gauss and the direction is 50° downward north. The optical cavity is orientated 30° northeast. Using the geometric relationship shown in Fig. 5, we obtained $\theta = 56^\circ$ and $\eta = 157^\circ$ for the experimental conditions in this work.

The Zeeman structure in an arbitrary magnetic field can be calculated with the above equations and those given in the Appendix. We simulated spectral envelopes of the ${}^PQ(10)$ transition under magnetic fields in different directions with the same amplitude of 0.55 Gauss. In two particular cases where the laser propagates in a parallel direction and perpendicularly to the magnetic field, as shown in Figs. 6(a) and 6(b), the spectra exhibit different characteristics. When the laser beam is parallel to the magnetic field, only $\sigma_\pm$ components are presented in the spectrum. When they are perpendicular, as shown in Fig. 6(b), only σ_π components are presented. Under the local geomagnetic field, the simulated spectrum is composed of 39% $\sigma_\pm$ and 61% π components, shown as the black solid line in Fig. 6(c). It agrees reasonably well with the experimental spectrum (red dots). Note that the simulation does not include crossovers [61] among different Zeeman subcomponents.

Under a given magnetic field, each transition in the A band of O_2 splits to multiple Zeeman components and the Zeeman shifts follow Eq. (2). We calculate the Zeeman splittings "d" under the magnetic field of 1.0 Gauss, using the g factors given in Ref. [37] where anisotropic spin, rotational, and spin-spin corrections to g factors are included. The results are shown in Fig. 7. For comparison, splittings based on a simplified Hund's case (b) model [54] are also given, and the differences between these two models are shown in the lower panel of Fig. 7 for different transitions. As we can see, the Zeeman splitting decreases rapidly with an increasing J value. Under the geomagnetic field in this work, the d value is below 0.1 MHz for transitions $J'' > 10$. That is the reason why the Zeeman components were unresolved in this work. However, it is possible to resolve the Zeeman components

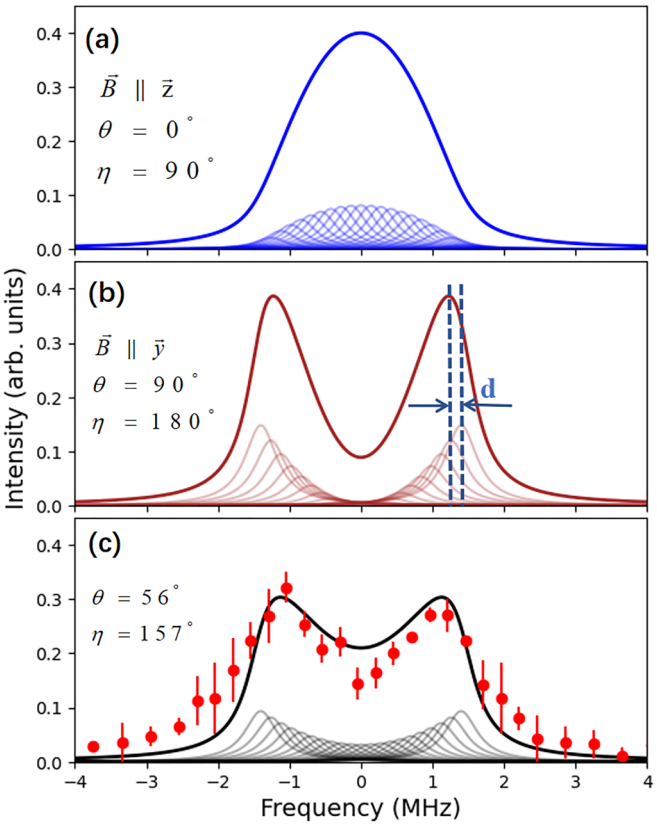

FIG. 6. Absorption spectra of $^{P}Q(10)$ under magnetic fields in different directions with the same amplitude of 0.55 Gauss. Bold solid lines show sums of all simulated Zeeman components (thin lines). (a) The magnetic field is parallel to the laser propagation direction (z), $\theta = 0^\circ$ and $\eta = 90^\circ$. (b) The magnetic field is perpendicular to the laser beam and parallel to the y direction, $\theta = 90^\circ$ and $\eta = 180^\circ$. The distance between two nearby Zeeman components is indicated as "d." (c) The local geomagnetic field, $\theta = 56^\circ$, and $\eta = 157^\circ$. Red scattering points with error bars are experimental data. Definition of the direction of the magnetic field is given in Fig. 5.

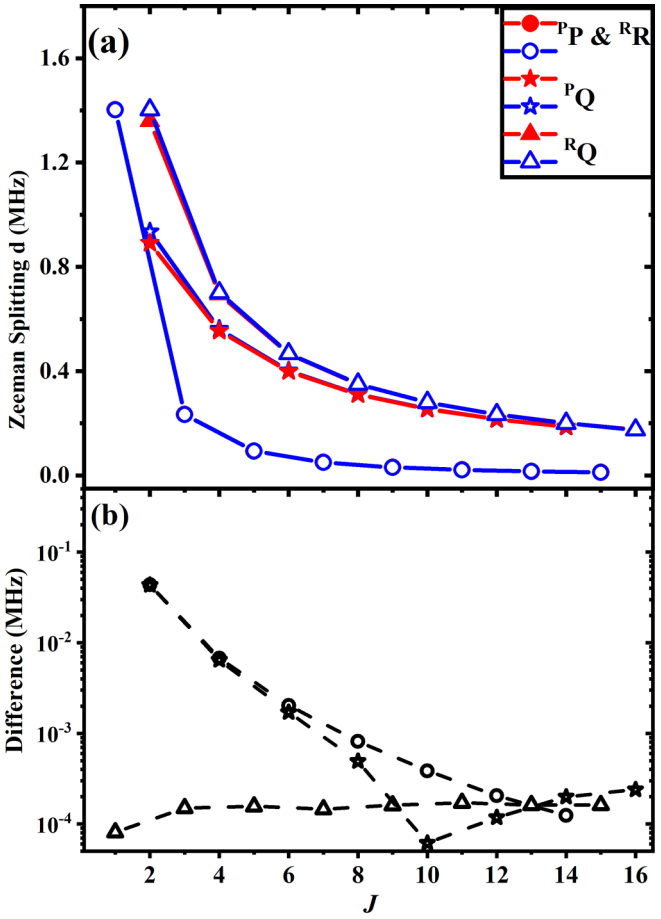

FIG. 7. (a) Calculated Zeeman splittings d under the magnetic field of 1.0 Gauss for transitions in the A band, using $g(J)$ values given by the models with [37] (red solid symbol) or without [54] (blue open symbol) corrections. (b) Differences between both values from two models.

by SAS measurements for low-J transitions. Moreover, as shown in the lower panel of Fig. 7, deviations due to the models with or without corrections calculating the $g(J)$ factors are significant for ^{P}Q and ^{R}Q transitions with low J values. Saturated absorption spectroscopy of these transitions may yield a determination of the $g(J)$ value with an accuracy at the 1% level if the magnetic field is also precisely measured, giving an experimental evaluation of the models. In turn, such a measurement could be used to assess the Zeeman effect on atmospheric temperature remote sensing profiles at high altitudes and allow applications in remote sensing of astrophysical magnetic fields. Unfortunately, these transitions are beyond the scanning range of the diode laser used in this work, and they will be studied in a succeeding work.

IV. CONCLUSION

This work presents a saturated absorption spectroscopy measurement of magnetic dipole ($M1$) transitions of molecules. Lamb dips of eight transitions around 764 nm in the P branch of the oxygen A band were observed. The spectral splittings caused by the Zeeman effect under the geomagnetic field for ^{P}Q transitions were partially resolved, which were analyzed using the Stokes formalism. Magnetic shielding was applied to reduce the influence of the geomagnetic field, which allows for determinations of line positions with an accuracy of a few kHz. The results in this study show that the oxygen Landé factors in the ground state $X\,^3\Sigma_g^-$ can be experimentally determined with the SAS measurements under a uniform magnetic field. Such Landé factors are of great importance in atmospheric remote sensing.

ACKNOWLEDGMENTS

This work was jointly supported by the National Natural Science Foundation of China (Grants No. 22273096, No. 11974328, and No. 21688102), the Ministry of Science and Technology of China (Grants No. 2021ZD0303102 and No. 2022YFF0606500), and the Strategic Priority Research Program of the Chinese Academy of Sciences (Grants No. XDC07010000 and No. XDB21020100).

APPENDIX: TRANSLATING THE PROPAGATION MATRIX

Stokes proposed [62] that the polarization and intensity of a laser beam can be described using four parameters, forming a four-dimensional column vector, which can be expressed as

$$\vec{S} = \begin{bmatrix} I \\ Q \\ U \\ V \end{bmatrix} = \begin{bmatrix} E_x^2 + E_y^2 \\ E_x^2 - E_y^2 \\ 2E_xE_y\cos\delta \\ 2E_xE_y\sin\delta \end{bmatrix}. \tag{A1}$$

Here, I is the total intensity of the light wave; Q describes the intensity difference between the x and y directions; U is the difference between the $+45^\circ$ and -45° polarization components; and V is the intensity difference between left- and right-circular components. After normalization, horizontally polarized light can be represented as $[1 \quad 1 \quad 0 \quad 0]^T$.

At the same time, polarized optical devices can be represented by a 4×4 matrix M, and the transformation characteristics can be expressed by a Mueller matrix [63]. The matrix to describe passing through a polarized beam splitter (PBS) can be written as

$$M = \frac{1}{2}\begin{bmatrix} 1 & 1 & 0 & 0 \\ 1 & 1 & 0 & 0 \\ 0 & 0 & 0 & 0 \\ 0 & 0 & 0 & 0 \end{bmatrix}. \tag{A2}$$

The matrix for absorption by oxygen molecules in a magnetic field is provided in Ref. [55]:

$$\Phi = \begin{bmatrix} \phi_I & \phi_Q & \phi_U & \phi_V \\ \phi_Q & \phi_I & \phi'_V & -\phi'_U \\ \phi_U & -\phi'_V & \phi_I & \phi'_Q \\ \phi_V & \phi'_U & -\phi'_Q & \phi_I \end{bmatrix},$$

$$\phi_I = \tfrac{1}{2}\phi_\pi \sin^2\theta + \tfrac{1}{4}(\phi_{\sigma_+} + \phi_{\sigma_-})(1 + \cos^2\theta),$$

$$\phi_Q = \tfrac{1}{2}\left[\phi_\pi - \tfrac{1}{2}(\phi_{\sigma_+} + \phi_{\sigma_-})\right]\sin^2\theta\cos 2\eta,$$

$$\phi_U = \tfrac{1}{2}\left[\phi_\pi - \tfrac{1}{2}(\phi_{\sigma_+} + \phi_{\sigma_-})\right]\sin^2\theta\sin 2\eta,$$

$$\phi_V = \tfrac{1}{2}(\phi_{\sigma_-} - \phi_{\sigma_+})\cos\theta,$$

$$\phi'_Q = \tfrac{1}{2}\left[\phi'_\pi - \tfrac{1}{2}(\phi'_{\sigma_+} + \phi'_{\sigma_-})\right]\sin^2\theta\cos 2\eta,$$

$$\phi'_U = \tfrac{1}{2}\left[\phi'_\pi - \tfrac{1}{2}(\phi'_{\sigma_+} + \phi'_{\sigma_-})\right]\sin^2\theta\sin 2\eta,$$

$$\phi'_V = \tfrac{1}{2}(\phi'_{\sigma_-} - \phi'_{\sigma_+})\cos\theta. \tag{A3}$$

In the above equations, terms ϕ and ϕ' represent absorption attenuation and the magnetooptical effect, respectively,

$$\phi_i = \sum_i S_i F(\nu, \nu_0 + \Delta\nu_0),$$

$$\phi'_i = \sum_i S_i F'(\nu, \nu_0 + \Delta\nu_0). \tag{A4}$$

The subscript i represents each Zeeman component. F and F' are the absorption line shape and magnetooptical line shape functions, respectively. Since the pressure broadening is dominant in our experiment, we use Lorentzian functions to describe the absorption line shapes for different Zeeman components. As for the magnetooptical line shapes, the Faraday-Voigt function is used [55]. However, in our subsequent theoretical analysis, the impact of polarization combinations does not exist in our theoretical model.

Therefore, the overall optical propagation process can be expressed as

$$\frac{1}{2}\begin{bmatrix} 1 & 1 & 0 & 0 \\ 1 & 1 & 0 & 0 \\ 0 & 0 & 0 & 0 \\ 0 & 0 & 0 & 0 \end{bmatrix}\begin{bmatrix} \phi_I & \phi_Q & \phi_U & \phi_V \\ \phi_Q & \phi_I & \phi'_V & -\phi'_U \\ \phi_U & -\phi'_V & \phi_I & \phi'_Q \\ \phi_V & \phi'_U & -\phi'_Q & \phi_I \end{bmatrix}\begin{bmatrix} 1 \\ 1 \\ 0 \\ 0 \end{bmatrix} = \begin{bmatrix} I \\ Q \\ U \\ V \end{bmatrix}. \tag{A5}$$

In our experimental configuration, we detected the total light intensity I, which is the sum of two terms: $I = \phi_I + \phi_Q$.

[1] R. F. Keeling, R. P. Najjar, M. L. Bender, and P. P. Tans, Global Biogeochem. Cycles **7**, 37 (1993).

[2] A. C. Manning and R. F. Keeling, Tellus B: Chem. Phys. Meteorol. **58**, 95 (2006).

[3] J. Huang, X. Liu, Y. He, S. Shen, Z. Hou, S. Li, C. Li, L. Yao, and J. Huang, Sci. China Earth Sci. **64**, 511 (2021).

[4] D. Atamanchuk, J. Koelling, U. Send, and D. W. R. Wallace, Nat. Geosci. **13**, 232 (2020).

[5] S. Ishidoya, K. Tsuboi, Y. Niwa, H. Matsueda, S. Murayama, K. Ishijima, and K. Saito, Atmos. Chem. Phys. **22**, 6953 (2022).

[6] B. Brumfield and G. Wysocki, Opt. Express **20**, 29727 (2012).

[7] E. J. Zhang, B. Brumfield, and G. Wysocki, Opt. Express **22**, 15957 (2014).

[8] J. Westberg and G. Wysocki, Appl. Phys. B: Lasers Opt. **123**, 168 (2017).

[9] J. Hayden, J. Westberg, C. L. Patrick, B. Lendl, and G. Wysocki, Opt. Lett. **43**, 5046 (2018).

[10] Q. Y. Yang, Y. Tan, Z.-H. Qu, Y. Sun, A.-W. Liu, and S.-M. Hu, Anal. Chem. **95**, 5652 (2023).

[11] K. Chance, J. Quant. Spectrosc. Radiat. Transfer **58**, 375 (1997).

[12] C. E. Miller, L. R. Brown, R. A. Toth, D. C. Benner, and V. M. Devi, C. R. Phys. **6**, 876 (2005).

[13] A. Kuze, H. Suto, M. Nakajima, and T. Hamazaki, Appl. Opt. **48**, 6716 (2009).

[14] Y. Liu, D. X. Yang, and Z. N. Cai, Chin. Sci. Bull. **58**, 1520 (2013).

[15] D. Wunch, G. C. Toon, J. F. L. Blavier, R. A. Washenfelder, J. Notholt, B. J. Connor, D. W. T. Griffith, V. Sherlock, and P. O. Wennberg, Philos. Trans. R. Soc. A **369**, 2087 (2011).

[16] D. Murtagh, U. Frisk, F. Merino, M. Ridal, A. Jonsson, J. Stegman, G. Witt, P. Eriksson, C. Jiménez, G. Megie *et al.*, Can. J. Phys. **80**, 309 (2002).

[17] M. J. Schwartz, W. G. Read, and W. Van Snyder, IEEE Trans. Geosci. Remote Sens. **44**, 1182 (2006).

[18] A. von Engeln, J. Langen, T. Wehr, S. Bühler, and K. Künzi, J. Geophys. Res.: Atmos. **103**, 31735 (1998).

[19] A. von Engeln and S. Bühler, J. Geophys. Res.: Atmos. **107**, ACL 12-1–ACL 12-15 (2002).

[20] O. Stähli, A. Murk, N. Kämpfer, C. Mätzler, and P. Eriksson, Atmos. Meas. Tech. **6**, 2477 (2013).

[21] A. A. Shvetsov, L. I. Fedoseev, D. A. Karashtin, O. S. Bol'Shakov, D. N. Mukhin, N. K. Skalyga, and A. M. Feigin, Radiophys. Quant. Electron. **53**, 321 (2010).

[22] F. Navas-Guzmán, N. Kämpfer, A. Murk, R. Larsson, S. A. Buehler, and P. Eriksson, Atmos. Meas. Tech. **8**, 1863 (2015).

[23] S. A. Buehler, J. Mendrok, P. Eriksson, A. Perrin, R. Larsson, and O. Lemke, Geosci. Model Dev. **11**, 1537 (2018).

[24] W. Krochin, F. Navas-Guzmán, D. Kuhl, A. Murk, and G. Stober, Atmos. Meas. Tech. **15**, 2231 (2022).

[25] W. Krochin, G. Stober, and A. Murk, IEEE J. Sel. Top. Appl. Earth Obs. Remote Sens. **15**, 5644 (2022).

[26] H. D. Babcock and L. Herzberg, Astrophys. J. **108**, 167 (1948).

[27] A. O'Keefe and D. A. G. Deacon, Rev. Sci. Instrum. **59**, 2544 (1988).

[28] D. J. Robichaud, J. T. Hodges, P. Masłowski, L. Y. Yeung, M. Okumura, C. E. Miller, and L. R. Brown, J. Mol. Spectrosc. **251**, 27 (2008).

[29] K. Bielska, S. Wójtewicz, P. Morzyński, P. Ablewski, A. Cygan, M. Bober, J. Domysławska, M. Zawada, R. Ciuryło, P. Masłowski, and D. Lisak, J. Quant. Spectrosc. Radiat. Transfer **201**, 156 (2017).

[30] D. K. Havey, D. A. Long, M. Okumura, C. E. Miller, and J. T. Hodges, Chem. Phys. Lett. **483**, 49 (2009).

[31] J. Domysławska, S. Wójtewicz, P. Masłowski, A. Cygan, K. Bielska, R. S. Trawiński, R. Ciuryło, and D. Lisak, J. Quant. Spectrosc. Radiat. Transfer **169**, 111 (2016).

[32] F. R. Spiering, M. B. Kiseleva, N. N. Filippov, H. Naus, B. van Lieshout, C. Weijenborg, and W. J. van der Zande, J. Chem. Phys. **133**, 114305 (2010).

[33] J. Domysławska, S. Wojtewicz, K. Bielska, S. Bilicki, R. Ciuryło, and D. Lisak, J. Chem. Phys. **156**, 084301 (2022).

[34] H. Naus, A. de Lange, and W. Ubachs, Phys. Rev. A **56**, 4755 (1997).

[35] F. M. J. Cozijn, M. L. Diouf, and W. Ubachs, Phys. Rev. Lett. **131**, 073001 (2023).

[36] R. Larsson, R. Ramstad, J. Mendrok, S. A. Buehler, and Y. Kasai, Geophys. Res. Lett. **40**, 5014 (2013).

[37] R. Larsson, B. Lankhaar, and P. Eriksson, J. Quant. Spectrosc. Radiat. Transfer **224**, 431 (2019).

[38] J. Wang, Y. R. Sun, L.-G. Tao, A.-W. Liu, and S.-M. Hu, J. Chem. Phys. **147**, 091103 (2017).

[39] H. Wu, C.-L. Hu, J. Wang, Y. R. Sun, Y. Tan, A.-W. Liu, and S.-M. Hu, Phys. Chem. Chem. Phys. **22**, 2841 (2020).

[40] L.-G. Tao, T.-P. Hua, Y. R. Sun, J. Wang, A.-W. Liu, and S.-M. Hu, J. Quant. Spectrosc. Radiat. Transfer **210**, 111 (2018).

[41] L.-S. Ma, J. Ye, P. Dubé, and J. L. Hall, J. Opt. Soc. Am. B **16**, 2255 (1999).

[42] I. E. Gordon, L. S. Rothman, R. J. Hargreaves, R. Hashemi, E. V. Karlovets, F. M. Skinner, E. K. Conway, C. Hill, R. V. Kochanov, Y. Tan, P. Wcisło, A. A. Finenko, K. Nelson, P. F. Bernath, M. Birk, V. Boudon, A. Campargue, K. V. Chance, A. Coustenis, B. J. Drouin, J.-M. Flaud *et al.*, J. Quant. Spectrosc. Radiat. Transfer **277**, 107949 (2022).

[43] G. Giusfredi, S. Bartalini, S. Borri, P. Cancio, I. Galli, D. Mazzotti, and P. De Natale, Phys. Rev. Lett. **104**, 110801 (2010).

[44] S. Twagirayezu, G. E. Hall, and T. J. Sears, J. Chem. Phys. **149**, 154308 (2018).

[45] Y. Tan, T.-P. Hua, J.-D. Tang, J. Wang, A.-W. Liu, Y. R. Sun, C.-F. Cheng, and S.-M. Hu, J. Phys.: Conf. Ser. **2439**, 012007 (2023).

[46] A. Predoi-Cross, K. Hambrook, R. Keller, C. Povey, I. Schofield, D. Hurtmans, H. Over, and G. C. Mellau, J. Mol. Spectrosc. **248**, 85 (2008).

[47] J. L. Hall, C. J. Bordé, and K. Uehara, Phys. Rev. Lett. **37**, 1339 (1976).

[48] S. Yu, B. J. Drouin, and C. E. Miller, J. Chem. Phys. **141**, 174302 (2014).

[49] M. A. Koshelev, G. Y. Golubiatnikov, I. N. Vilkov, and M. Y. Tretyakov, J. Quant. Spectrosc. Radiat. Transfer **278**, 108001 (2022).

[50] S. V. Berdyugina and S. K. Solanki, Astron. Astrophys. **385**, 701 (2002).

[51] A. Hinz, J. Pfeiffer, W. Bohle, and W. Urban, Mol. Phys. **45**, 1131 (1982).

[52] J. J. Kankare and R. Stephens, Spectrochim. Acta, Part B **35**, 849 (1980).

[53] W. B. Lenoir, J. Appl. Phys. **38**, 5283 (1967).

[54] W. B. Lenoir, J. Geophys. Res. **73**, 361 (1968).

[55] R. Larsson, S. A. Buehler, P. Eriksson, and J. Mendrok, J. Quant. Spectrosc. Radiat. Transfer **133**, 445 (2014).

[56] J. Jefferies, B. W. Lites, and A. Skumanich, Astrophys. J. **343**, 920 (1989).

[57] S. V. Berdyugina, S. K. Solanki, and C. Frutiger, Astron. Astrophys. **412**, 513 (2003).

[58] P. Judge, M. Rempel, R. Ezzeddine, L. Kleint, R. Egeland, S. V. Berdyugina, T. Berger, P. Bryans, J. Burkepile, R. Centeno, G. de Toma, M. Dikpati, Y. Fan, H. Gilbert, and D. A. Lacatus, Astrophys. J. **917**, 27 (2021).

[59] S. A. Buehler, P. Eriksson, T. Kuhn, A. von Engeln, and C. Verdes, J. Quant. Spectrosc. Radiat. Transfer **91**, 65 (2005).

[60] P. Eriksson, S. A. Buehler, C. P. Davis, C. Emde, and O. Lemke, J. Quant. Spectrosc. Radiat. Transfer **112**, 1551 (2011).

[61] W. Demtröder, *Laser Spectroscopy Vol. 2: Experimental Techniques* (Springer, Berlin, 2008), pp. 77–139.

[62] W. H. McMaster, Rev. Mod. Phys. **33**, 8 (1961).

[63] R. Hui and M. O'Sullivan, *Fiber Optic Measurement Techniques* (Academic, Boston, 2009), pp. 365–479.